

High-order Tensor Pooling with Attention for Action Recognition

Piotr Koniusz^{§,†} Lei Wang^{†,§} Ke Sun^{§,†}
[†]Australian National University, [§]Data61/CSIRO
[§]firstname.lastname@data61.csiro.au

Abstract

We aim at capturing high-order statistics of feature vectors formed by a neural network, and propose end-to-end second- and higher-order pooling to form a tensor descriptor. Tensor descriptors require a robust similarity measure due to low numbers of aggregated vectors and the burstiness phenomenon, when a given feature appears more/less frequently than statistically expected. The Heat Diffusion Process (HDP) on a graph Laplacian is closely related to the Eigenvalue Power Normalization (EPN) of the covariance/auto-correlation matrix, whose inverse forms a loopy graph Laplacian. We show that the HDP and the EPN play the same role, i.e., to boost or dampen the magnitude of the eigenspectrum thus preventing the burstiness. We equip higher-order tensors with EPN which acts as a spectral detector of higher-order occurrences to prevent burstiness. We also prove that for a tensor of order r built from d dimensional feature descriptors, such a detector gives the likelihood if at least one higher-order occurrence is ‘projected’ into one of $\text{binom}(d,r)$ subspaces represented by the tensor; thus forming a tensor power normalization metric endowed with $\text{binom}(d,r)$ such ‘detectors’. For experimental contributions, we apply several second- and higher-order pooling variants to action recognition, provide previously not presented comparisons of such pooling variants, and show state-of-the-art results on HMDB-51, YUP++ and MPII Cooking Activities.

1. Introduction

Auto-correlation/covariance and higher-order tensor descriptors have been applied to many deep learning tasks, e.g., object, texture and action recognition, tracking and segmentation [43, 36, 31, 3]. A seminal approach [43] aggregates multiple low level feature vectors (that capture various directional gradient statistics) extracted from image regions to form a covariance matrix which is then used as a datapoint for a nearest neighbor retrieval or training an SVM classifier. Such covariance descriptors have been used in object classification, tracking, and so on

[43, 36, 56, 31, 19].

The role of pooling is to aggregate local feature descriptors extracted from an instance-to-classify, e.g., image patch, subsequence or subgraph descriptors from an image, video or a graph, respectively, into a single descriptor according to some statistically meaningful operation that encourages invariance w.r.t. the order of local descriptors, preserves useful global statistics, and is constant in its dimensionality (local descriptor counts do not affect the size of aggregated descriptor). Examples of pooling include average and max-pooling [2] often used with a sparse encoder. Second-order co-occurrence pooling, a strategy shown to result in a superior performance in semantic segmentation and visual concept detection compared to the first-order pooling [3, 26], is performed by aggregating the outer product of some intermediate feature vectors extracted by an encoder (e.g., the output of last convolutional layer in CNN) over image regions or video frames. A natural extension led to higher-order descriptors [26, 23, 25], e.g., third-order super-symmetric tensors (trilinear pooling) which improve results over the second-order descriptors (bilinear pooling) over 7% MAP on the PASCAL VOC07 challenge.

Tensor descriptors require an appropriate aggregation/pooling mechanism to obtain robust estimates of covariance, auto-correlation or higher-order statistics and tackle the problem of *burstiness*, a phenomenon that certain features may occur rarely or frequently in instances to classify but only a mere detection of presence/absence of a feature is relevant to the classification task. For instance, a CNN filter responding by a feature activation to a stimulus such as a tree leaf may respond once, few or many times across different spatial regions depending on whether a part or an entire tree is present in an image. However, reliably detecting a leaf (or few leaves), not the quantity per se, is a robust predictor of a tree [26]. Furthermore, presenting a classifier with varying counts of a feature makes it simply harder for the classifier to generalize to unseen instances, e.g., if training images contained a small part of a tree (few leaves shown), it is likely that test images containing entire trees (thousands of leaves) will be misclassified as the decision boundary of a classifier is sensitive to

the observed feature counts. For this reason, higher-order representations undergo a non-linearity such as Power Normalization (PN) [26, 23, 27] which role is to reduce/boost contributions from frequent/infrequent visual stimuli in an image, respectively. Similar mechanisms apply to the temporal domain/action classification [25]. PN methods can be split into element- and spectrum-wise, the latter referred to as Eigenvalue Power Normalization (EPN) [26].

So-called MaxExp and Gamma are two superior EPN operators with state-of-the-art performance [26, 28, 27]. Thus, we perform a theoretical analysis of such EPN operators along with an application to action recognition.

Our contributions are summarized as follows:

1. As MaxExp, Gamma and HDP can be thought of as pushforward functions acting on the discrete distribution representing an eigenspectrum, both MaxExp and Gamma are upper bounds of HDP, and MaxExp and Gamma can indeed be formulated as a modified system of Ordinary Differential Equations (ODE) defining the Heat Diffusion Equation [27], we show that Gamma is equal to HDP on the Log-Euclidean maps [1]. We note that MaxExp, Gamma and HDP are approximations of the Grassmann metric [20] which helps us design our spectral detector detailed next.
2. EPN has been long speculated [26] to perform spectral detection of higher-order occurrences. We prove that a tensor of order r , built from d dimensional feature vectors, coupled with MaxExp indeed detects and yields the likelihood if at least one higher-order occurrence is ‘projected’ into one of $\binom{d}{r}$ subspaces of dimension r represented by the tensor; thus forming a Tensor Power Normalization metric endowed with $\binom{d}{r}$ such ‘detectors’.
3. Additionally, we show how to backpropagate through the Higher Order Singular Value Decomposition (HOSVD) defined in [30, 22], which is essential in higher-order descriptors with EPN.

As EPN prevents burstiness, it replaces counting correlated features with detecting them, thus being invariant to their spatial/temporal extent.

2. Eigenvalue Power Normalization

This section provides the prerequisites on power normalization methods of high dimensional tensors.

Notations. $\mathcal{X} \in \mathbb{R}^{d_1 \times d_2 \times \dots \times d_r}$ denotes r -order tensor. By default $r = 3$ meaning that \mathcal{X} is a third-order tensor with exceptions depending on the context. The i -th slice of this tensor is denoted as $\mathcal{X}_{:, :, i}$, which is a $d_1 \times d_2$ matrix. For a matrix $\mathbf{X} \in \mathbb{R}^{d_1 \times d_2}$ and a vector $\mathbf{x} = (x_1, \dots, x_{d_3}) \in \mathbb{R}^{d_3}$, $\mathcal{X} = \mathbf{X} \uparrow \otimes \mathbf{x}$ gives a tensor $\mathcal{X} \in \mathbb{R}^{d_1 \times d_2 \times d_3}$, where the i -th slice of \mathcal{X} is given by $\mathbf{X} \cdot x_i$. A symmetric third-order tensor of rank one $\mathcal{X} \in \mathbb{R}^{d \times d \times d}$ can be obtained

from \mathbf{x} as $\mathcal{X} = \uparrow \otimes_3 \mathbf{x} \triangleq (\mathbf{x} \mathbf{x}^T) \uparrow \otimes \mathbf{x}$. $\mathcal{X} = \uparrow \otimes_r \mathbf{x}$ means the r -order outer product of \mathbf{x} , where the (i_1, \dots, i_r) -th coefficient of \mathcal{X} is given by $\mathcal{X}_{i_1, \dots, i_r} = x_{i_1} \cdot x_{i_2} \dots \cdot x_{i_r}$. The Frobenius norm of a tensor \mathcal{X} is given by $\|\mathcal{X}\|_F = \sqrt{\sum_{i,j,k} \mathcal{X}_{ijk}^2}$, where \mathcal{X}_{ijk} represents the ijk -th element of \mathcal{X} . Similarly, the inner-product between two tensors \mathcal{X} and \mathcal{Y} is given by $\langle \mathcal{X}, \mathcal{Y} \rangle = \sum_{ijk} \mathcal{X}_{ijk} \mathcal{Y}_{ijk}$. The tensor product \times_j in mode j between $\mathcal{X} \in \mathbb{R}^{d_1 \times d_2 \times \dots \times d_r}$ and $\mathcal{Y} \in \mathbb{R}^{d'_1 \times d'_2 \times \dots \times d'_r}$, where $d_j = d'_j$, is denoted as $\mathcal{X} \times_j \mathcal{Y} \in \mathbb{R}^{d_1 \times \dots \times d_{j-1} \times d_{j+1} \times \dots \times d_r \times d'_1 \times \dots \times d'_{j-1} \times d'_{j+1} \times \dots \times d'_r}$. The $(i_1, \dots, i_{j-1}, i_{j+1}, \dots, i_r, i'_1, \dots, i'_{j-1}, i'_{j+1}, \dots, i'_r)$ -th coefficient of $\mathcal{X} \times_j \mathcal{Y}$ is given by $\sum_{i_j} \mathcal{X}_{i_1, \dots, i_j, \dots, i_r} \cdot \mathcal{Y}_{i'_1, \dots, i'_j, \dots, i'_r}$. We denote the spaces of $d \times d$ Symmetric Positive Semi-Definite (SPSD) and Symmetric Positive Definite (SPD) matrices as \mathcal{S}_+^d and \mathcal{S}_{++}^d , \mathcal{I}_r is an index sequence $1, 2, \dots, r$, \mathbf{I} is the identity matrix, \dagger is a Moore–Penrose inverse, $\{e_i : i \in \mathcal{I}_d\}$ are the spanning bases of \mathbb{R}^d . Bold lowercase/uppercase letters denote vectors/matrices, bold uppercase mathcal letters denote tensors, and regular letters denote scalars.

Tensor Pooling. The following proposition formalizes the notion of higher-order descriptors.

Proposition 1 ([24]). *Let $\Phi \equiv \{\phi_1, \dots, \phi_N \in \mathbb{R}^d\}$ and $\Phi^* \equiv \{\phi_1^*, \dots, \phi_M^* \in \mathbb{R}^d\}$ be feature vectors extracted from two instances to classify, e.g., video sequences, images, text documents, etc. Let $\mathbf{w} \in \mathbb{R}_+^N$, $\mathbf{w}^* \in \mathbb{R}_+^M$ be some non-negative weights and $\boldsymbol{\mu}, \boldsymbol{\mu}^* \in \mathbb{R}^d$ be the mean vectors of Φ and Φ^* , respectively. A linearization of the sum of polynomial kernels of degree r*

$$\langle \mathcal{X}(\Phi; \mathbf{w}, \boldsymbol{\mu}), \mathcal{X}(\Phi^*; \mathbf{w}^*, \boldsymbol{\mu}^*) \rangle$$

$$= \frac{1}{NM} \sum_{n=1}^N \sum_{m=1}^M w_n^r w_m^{*r} \langle \phi_n - \boldsymbol{\mu}, \phi_m^* - \boldsymbol{\mu}^* \rangle^r,$$

yields the tensor feature map

$$\mathcal{X}(\Phi; \mathbf{w}, \boldsymbol{\mu}) = \frac{1}{N} \sum_{n=1}^N w_n^r \uparrow \otimes_r (\phi_n - \boldsymbol{\mu}) \in \mathbb{R}^{d \times d \times \dots \times d}. \quad (2)$$

Φ and Φ^* do not have to be zero-mean centered ($\boldsymbol{\mu} = \boldsymbol{\mu}^* = 0$) if one uses an auto-correlation matrix/tensor instead of covariance. The weights \mathbf{w} and \mathbf{w}^* can differ for each feature vector, e.g., they may be the same within each group of feature vectors (image patch, video subsequence) but differ across different groups (patches of different sizes or subsequences of different lengths).

The EPN [26] performs a spectrum transformation on a given higher-order descriptor $\mathcal{X} \in \mathbb{R}^{d_1 \times d_2 \times \dots \times d_r}$, as detailed in the following steps

$$(\lambda; U_1, \dots, U_r) = \text{HOSVD}(\mathcal{X}), \quad (3)$$

$$\hat{\lambda} = g(\lambda), \quad (4)$$

$$\mathcal{G}(\mathcal{X}) = ((\hat{\lambda} \times_1 U_1) \dots) \times_r U_r, \quad (5)$$

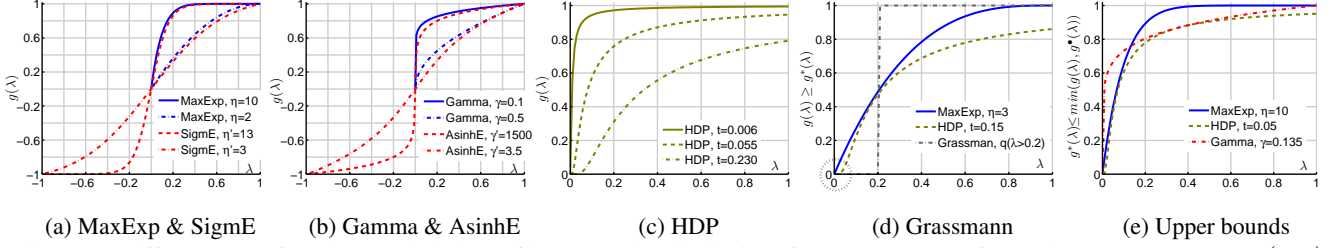


Figure 1: Different EPN functions and their profiles. Note the similarity of MaxExp ($\eta > 1$) from Fig. 1a, Gamma ($\gamma \in (0, 1)$) from Fig. 1b and HDP ($t \in (0, 1)$) from Fig. 1c to each other. Also, the circle in Fig. 1d highlights the region where the profile of HDP differs from MaxExp. Furthermore, note that the above EPN functions are soft approximations of the Grassmann map (the step function) in Fig. 1d. Finally, Fig. 1e shows that MaxExp and Gamma given by $g(\lambda)$ and $g^\bullet(\lambda)$ are upper bounds of HDP given by $g^*(\lambda)$ (see details in [27]).

where HOSVD stands for Higher Order Singular Value Decomposition [30, 22], the small-case g acts on the so-called core tensor $\lambda \in \mathbb{R}^{d'_1 \times d'_2 \times \dots \times d'_r}$ in an element-wise manner, where $d'_i \leq d_i, \forall i$, and $\hat{\lambda} \in \mathbb{R}^{d'_1 \times d'_2 \times \dots \times d'_r}$ is the power-normalized counterpart of λ . Moreover, $\{U_i \in \mathbb{R}^{d_i \times d'_i}\}_{i \in \mathcal{I}_r}$ are r singular vector matrices. The uppercase mathematical notation indicates that \mathcal{G} is a spectrum-wise (*c.f.* element-wise) operator on \mathcal{X} . As the input tensor \mathcal{X} is *super-symmetric* by Eq. (2), *i.e.*, we have $\mathcal{X}_{i_1, i_2, \dots, i_r} = \mathcal{X}_{\Pi(i_1, i_2, \dots, i_r)}$ for any indexes (i_1, i_2, \dots, i_r) and any permutation Π , thus we have $U_1 = U_2 = \dots = U_r$.

Popular variants of EPN pooling [28, 27] shown in Fig. 1, are given below, two for SPD/SPSD matrices and two for indefinite matrices (Krein spaces):

Gamma $g(\lambda; \gamma) = \lambda^\gamma$ (*e.g.*, $\lambda^{\frac{1}{2}}$), in matrix form, $\mathcal{G}(\mathbf{X}; \gamma) = \mathbf{X}^\gamma$ (*e.g.*, $\mathbf{X}^{\frac{1}{2}}$ *a.k.a.* matrix square root).

MaxExp $g(\lambda; \eta) = 1 - (1 - \lambda)^\eta$, in matrix form, $\mathcal{G}(\mathbf{X}; \eta) = \mathbb{I} - (\mathbb{I} - \mathbf{X})^\eta$.

AsinhE $g(\lambda; \gamma') = \text{Arcsinh}(\gamma' \lambda)$ and $\mathcal{G}(\mathbf{X}; \gamma') = \text{Log}(\gamma' \mathbf{X} + (\mathbb{I} + \gamma'^2 \mathbf{X}^2)^{\frac{1}{2}})$. AsinhE is the Arcus Hyperbolic Sine function.

SigmE $g(\lambda; \eta') = 2/(1 + e^{-\eta' \lambda}) - 1$ and $\mathcal{G}(\mathbf{X}; \eta') = 2(\mathbb{I} + \text{Exp}(-\eta' \mathbf{X}))^{-1} - \mathbb{I}$. SigmE stands for a zero-centered Logistic *a.k.a.* Sigmoid function.

As shown in Figures 1a and 1b, SigmE/AsinhE extend Gamma/MaxExp to Krein spaces by reflecting function Gamma/MaxExp defined for non-negative eigenvalues λ by the vertical symmetry axis followed by the change of sign. Parameters $0 < \gamma \leq 1, \eta \geq 1, 0 < \gamma' \leq 1$ and $\eta' \geq 1$ control effect/steepness of such non-linearities. Moreover, eigenvalues λ are typically normalized by $\sum_i |\lambda_i|$ and therefore $\forall i, -1 \leq \lambda_i \leq 1$. Figures 1c and 1d show the impact of PN by varying γ of Gamma. Figure 1d shows that Gamma performs whitening/evening out the spectrum of $\mathbf{X} \in \mathbb{R}^{d \times d}$.

The EPN induces a family of non-Euclidean distance $\|\mathcal{G}(\mathcal{X}) - \mathcal{G}(\mathcal{Y})\|_F$ in the SPSP/SPD cone. The Power-Euclidean (PowE) metric $\frac{1}{\gamma} \|\mathbf{X}^\gamma - \mathbf{Y}^\gamma\|_2$ is discussed by [12] who point out that as $\gamma \rightarrow 0$, the Power-Euclidean metric converges to the Log-Euclidean (LogE) metric $\|\text{Log}(\mathbf{X}) - \text{Log}(\mathbf{Y})\|_F$. Matrix Square Root (MSR) based distance is in fact close to the Cholesky-Euclidean (CholE) distance $\|\text{Chol}(\mathbf{X}) - \text{Chol}(\mathbf{Y})\|_F$ suggested by [12]. However, the best results for Power-Euclidean distance (whose underlying feature map is Gamma) are typically attained with $0 \ll \gamma \neq 0.5$ [32, 28], which means the above connections to the Log-Euclidean metric and ‘robust covariance estimation’ are somewhat loose. Gamma for element-wise matrix pooling (*c.f.* spectral/eigenvalue pooling) is connected [28] to an operator called MaxExp. Intuitively, MaxExp yields ‘the probability of at least one co-occurrence event ($\phi_n \cap \phi'_n = 1$) occurring in ϕ_n and ϕ'_n simultaneously, given $N \approx \eta$ Bernoulli trials and two event vectors $\phi, \phi' \in \{0, 1\}^N$. In fact, element-wise MaxExp/Gamma have similar profiles as Fig. 1 shows. As EPN whitens the eigenspectrum of signal, it also differs from the batch normalization of variance of gradient features.

3. Main Results

We show that MaxExp is a spectral detector and formulate the capacity of tensor descriptors to perform subspace-based detection thus providing a robust Tensor Power Normalization metric to tackle the burstiness problem. Below, we derive of eigenvalue/spectral MaxExp. First, we establish its connection to Grassmann maps. Figure 1d shows a pooling operator g realizing the Grassmann feature map¹ whose step function suggest it can act as a detector. Remark below details how to obtain Grassmann maps.

Remark 1. Assume we have top q largest eigenvalues of \mathbf{X} with the corresponding eigenvectors and $q <$

¹Grassmann maps are not used in the reminder of this paper as they approximate HDP worse than MaxExp (Figure 1d). Grassmann maps also yielded lower accuracies than MaxExp in our preliminary experiments.

$\min(\text{Rank}(\mathbf{X}_1), \dots, \text{Rank}(\mathbf{X}_M))$ for the total of M covariance descriptors. Then, the pooling operator $g(\boldsymbol{\lambda}, q) = [[1]_{i \in \mathcal{I}_q}, [0]_{i \in \mathcal{I}_{d-q}}]^T$ where 1 is repeated q times in the vector followed by 0 repeated $d-q$ times, realizes the feature map used in computations the Grassmann distance, that is $\mathcal{G}(\mathbf{X}) = \mathbf{U} \text{diag}(g(\boldsymbol{\lambda})) \mathbf{U}^T$, \mathbf{U} contains sorted eigenvectors of \mathbf{X} (descending order of eigenvalues).

In the reminder of this section, we establish the derivation of MaxExp in the spectral setting for Higher-order Tensors (HoT). We show that third-order tensor descriptors combined with MaxExp outperform second-order descriptors. For a probability density $f_X(\mathbf{x})$, its characteristic function $\varphi_X = \mathbb{E}(\exp(jX\omega)) = \sum_{i=0}^{\infty} \frac{j^i}{i!} \mathbb{E}(X^i) \omega^i$, where X^i is essentially our \mathcal{X} of order i in Eq. (6). If one could reliably estimate \mathcal{X} for $i = 0, \dots, \infty$, the underlying $f_X(\mathbf{x})$ can be found too. However, estimating just a single $\mathbb{E}(X^i)$, e.g., second- or third-order statistics, poses a choice between using (i) a less informative lower-order statistical moment $\mathbb{E}(X^2)$ but easier to estimate (matrix grows quadratically with d) vs. (ii) a more informative higher-order moment whose size explodes (e.g., cubically w.r.t. d for third-order tensors) thus requiring more data for robust estimations. By tackling the burstiness, our EPN helps estimate the HoT descriptors more robustly.

3.1. HoT with EPN

Below, we show that EPN in fact retrieves factors which quantify whether there is at least one datapoint $\phi_n, n \in \mathcal{I}_N$, projected into each subspace spanned by r -tuples of eigenvectors from matrices $\mathbf{U}_1 = \mathbf{U}_2 = \dots = \mathbf{U}_r$. For brevity, assume order $r = 3$, a super-symmetric tensor, and any 3-tuple of eigenvectors \mathbf{u}, \mathbf{v} , and \mathbf{w} from \mathbf{U} . Note that $\mathbf{u} \perp \mathbf{v}, \mathbf{v} \perp \mathbf{w}$ and $\mathbf{u} \perp \mathbf{w}$ due to orthogonality of eigenvectors for super-symmetric tensors, e.g., $\mathbf{U} \boldsymbol{\lambda}^\dagger \mathbf{V} = [\mathcal{X}_{::,1}, \dots, \mathcal{X}_{::,d}] \in \mathbb{R}^{d \times d^2}$ where $\boldsymbol{\lambda}^\dagger$ are eigenvalues of the unfolded tensor \mathcal{X} (note that they are not the core tensor of \mathcal{X} obtained by the HOSVD, which we denote as $\boldsymbol{\lambda}$). Moreover, note that if we have d unique eigenvectors, we can enumerate $\binom{d}{r}$ r -tuples and thus $\binom{d}{r}$ subspaces $\mathbb{R}^{d \times r} \subset \mathbb{R}^{d \times d}$. For simplicity, we assume we have d such vectors, that is $d = \text{Rank}(\mathcal{X}_{::,i}), \forall i \in \mathcal{I}_d$, otherwise if $d' < d$, then we would have $\binom{d'}{r}$ subspaces instead. For brevity, let $\|\phi\|_2 = 1$ and $\phi \geq 0$. Also, we write ϕ_n instead of ϕ for $n \in \mathcal{I}_N$ when index n matters. Firstly, let us remove weights and zero-mean centering of our super-symmetric tensor descriptor from Eq. (2):

$$\mathcal{X} = \frac{1}{N} \sum_{n \in \mathcal{I}_N} \uparrow \otimes_r \phi_n, \quad (6)$$

and write the ‘diagonalization’ of \mathcal{X} by eigenvectors \mathbf{u}, \mathbf{v} , and \mathbf{w} , which produces the core tensor with factors (spectrum of \mathcal{X}):

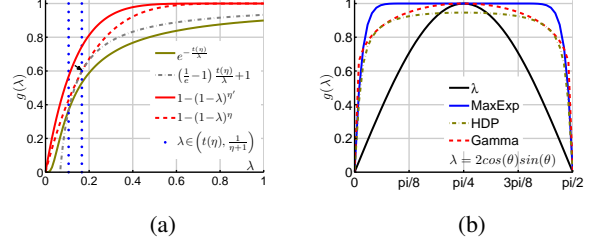


Figure 2: In Fig. 2a, the blue dashed lines indicate the range for which we provide bounds (see details in [27]). Imagine ‘lowering down’ MaxExp onto HDP (black arrow). Figure 2b simulates a single detection, an assignment into a subspace ($r=2$). $\theta \approx 0$ and $\theta \approx \pi/2$ simulate the case when the majority of feature descriptors fall close to the subspace boundary.

$$\lambda_{\mathbf{u}, \mathbf{v}, \mathbf{w}} = \mathcal{X} \times_1 \mathbf{u} \times_2 \mathbf{v} \times_3 \mathbf{w}, \quad (7)$$

where $\lambda_{\mathbf{u}, \mathbf{v}, \mathbf{w}}$ is a coefficient from the core tensor $\boldsymbol{\lambda}$ corresponding to eigenvectors \mathbf{u}, \mathbf{v} , and \mathbf{w} . Now, let us combine Eq. 6 and 7 which yields:

$$\begin{aligned} \lambda_{\mathbf{u}, \mathbf{v}, \mathbf{w}} &= \frac{1}{N} \sum_{n \in \mathcal{I}_N} \uparrow \otimes_3 \phi_n \times_1 \mathbf{u} \times_2 \mathbf{v} \times_3 \mathbf{w} \\ &= \frac{1}{N} \sum_{n \in \mathcal{I}_N} \langle \phi_n, \mathbf{u} \rangle \langle \phi_n, \mathbf{v} \rangle \langle \phi_n, \mathbf{w} \rangle. \end{aligned} \quad (8)$$

Theorem 1. Let ϕ_n be ‘optimally’ projected into subspace spanned by \mathbf{u}, \mathbf{v} and \mathbf{w} when $\psi'_n = \langle \phi_n, \mathbf{u} \rangle \langle \phi_n, \mathbf{v} \rangle \langle \phi_n, \mathbf{w} \rangle$ is maximized. As our \mathbf{u}, \mathbf{v} , and \mathbf{w} are orthogonal w.r.t. each other and $\|\phi_n\|_2 = 1$, simple Lagrange Eq. $\mathcal{L} = \Pi_{i=1}^r \mathbf{e}_i^T \phi_n + \lambda(\|\phi_n\|_2^2 - 1)$ yields maximum of $\kappa = (1/\sqrt{r})^r$ at $\phi_n = [(1/\sqrt{r}), \dots, (1/\sqrt{r})]^T$. For each $n \in \mathcal{I}_N$, we store $\psi_n = \psi'_n / \kappa$ in a so-called event vector ψ .

Assume that $\psi \in \{0, 1\}^N$ stores N outcomes of drawing from Bernoulli distribution under the i.i.d. assumption for which the probability p of an event ($\psi_n = 1$) and $1-p$ for ($\psi_n = 0$) are estimated by an expected value, $p = \text{avg}_n \psi_n = \lambda_{\mathbf{u}, \mathbf{v}, \mathbf{w}} / \kappa$ ($0 \leq \psi \leq 1$ in reality, $\lambda_{\mathbf{u}, \mathbf{v}, \mathbf{w}}, \kappa$ are introduced below in Eq. (8)). Then the probability of at least one projection event ($\psi_n = 1$) into the subspace spanned by r -tuples in N trials is:

$$\hat{\lambda}_{\mathbf{u}, \mathbf{v}, \mathbf{w}} = 1 - (1-p)^N = 1 - \left(1 - \frac{\lambda_{\mathbf{u}, \mathbf{v}, \mathbf{w}}}{\kappa}\right)^N. \quad (9)$$

Each of $\binom{d}{r}$ subspaces spanned by r -tuples acts as a detector of projections into this subspace. Eq. (9) is the spectral MaxExp pooling with κ normalization. Figure 2b simulates a detector by defining $\lambda_{\mathbf{u}, \mathbf{v}}$ from Eq. (8) as the cosine distance explicitly, that is $\lambda_{\mathbf{u}, \mathbf{v}} = \kappa \cos(\theta) \sin(\theta)$, $\kappa = 2$. Note the detector-like responses of MaxExp, Gamma and HDP.

Remark 2. We note that the event vector ψ may contain negative values, so extending Eq. (9) to

$\text{Sgn}(\lambda_{\mathbf{u},\mathbf{v},\mathbf{w}}) \left(1 - (1 - \frac{|\lambda_{\mathbf{u},\mathbf{v},\mathbf{w}}|}{\kappa})^\eta\right)$, where $\eta \approx N$, divides each of $\binom{d}{r}$ subspaces into ‘positive’ and ‘negative’ parts, η compensates for non-binary values in event vectors ψ . However, the above extension has a non-smooth derivative. Thus, we use in practice the smooth *SigME* operator defined in our introduction as $2 / \left(1 + e^{-\eta' \frac{|\lambda_{\mathbf{u},\mathbf{v},\mathbf{w}}|}{\kappa}}\right) - 1 \approx \text{Sgn}(\lambda_{\mathbf{u},\mathbf{v},\mathbf{w}}) \left(1 - (1 - \frac{|\lambda_{\mathbf{u},\mathbf{v},\mathbf{w}}|}{\kappa})^\eta\right)$ (assume some correct choice of η' given η). As third-order tensors are indefinite, *SigME* is a good choice as it works with Krein spaces by design, is smooth and almost indistinguishable from *MaxExp* (see Figure 1b).

Finally, consider the dot-product between EPN-norm. tensors $\mathcal{G}(\mathcal{X})$ and $\mathcal{G}(\mathcal{Y})$ computed by Eq. (3-5):

$$\begin{aligned} & \langle \mathcal{G}(\mathcal{X}), \mathcal{G}(\mathcal{Y}) \rangle \\ &= \sum_{\substack{\mathbf{u} \in U(\mathcal{X}) \\ \mathbf{v} \in V(\mathcal{X}) \\ \mathbf{w} \in W(\mathcal{X})}} \sum_{\substack{\mathbf{u}' \in U(\mathcal{Y}) \\ \mathbf{v}' \in V(\mathcal{Y}) \\ \mathbf{w}' \in W(\mathcal{Y})}} \hat{\lambda}_{\mathbf{u},\mathbf{v},\mathbf{w}} \hat{\lambda}'_{\mathbf{u}',\mathbf{v}',\mathbf{w}'} \langle \mathbf{u}, \mathbf{u}' \rangle \langle \mathbf{v}, \mathbf{v}' \rangle \langle \mathbf{w}, \mathbf{w}' \rangle. \end{aligned} \quad (10)$$

Hence, all subspaces of \mathcal{X} and \mathcal{Y} spanned by r -tuples (3-tuples in this example) are compared against each other for alignment by the cosine distance. When two subspaces $[\mathbf{u}, \mathbf{v}, \mathbf{w}]^T$ and $[\mathbf{u}', \mathbf{v}', \mathbf{w}']^T$ are aligned well, for a strong similarity between these subspaces to be yielded, a detection of at least one ϕ_n and ϕ'_n in these subspaces evidenced by $\hat{\lambda}_{\mathbf{u},\mathbf{v},\mathbf{w}}$ and $\hat{\lambda}'_{\mathbf{u}',\mathbf{v}',\mathbf{w}'}$ is also needed. We call Eq. (10) together with Eq. (3-5) as Tensor Power Euclidean (TPE) dot-product with associated Tensor Power Euclidean metric $\|\mathcal{X} - \mathcal{Y}\|_G = \|\mathcal{G}(\mathcal{X}) - \mathcal{G}(\mathcal{Y})\|_F$.

3.2. Backpropagating through HOSVD and/or SVD

To backpropagate through HOSVD, eigenvector matrices of \mathcal{X} , e.g., U_1, \dots, U_3 for the third order, are given by $U_1 \lambda_1^\dagger V_1 = M_1 = [\mathcal{X}_{:, :, 1}, \dots, \mathcal{X}_{:, :, d}] \in \mathbb{R}^{d \times d^2}$, $U_2 \lambda_2^\dagger V_2 = M_2 = [\mathcal{X}_{:, 1, :}, \dots, \mathcal{X}_{:, d, :}] \in \mathbb{R}^{d \times d^2}$ and $U_3 \lambda_3^\dagger V_3 = M_3 = [\mathcal{X}_{1, :, :}, \dots, \mathcal{X}_{d, :, :}] \in \mathbb{R}^{d \times d^2}$. M_1, \dots, M_3 are simply unfolded matrices of \mathcal{X} along the 1st, 2nd, and 3rd mode.

Proposition 2. Let $M^\# = MM^T = U\lambda U^T$ be an SPD matrix with simple eigenvalues, i.e., $\lambda_{ii} \neq \lambda_{jj}, \forall i \neq j$. Then U coincides also with the eigenvector matrix of tensor \mathcal{X} for the given unfolding. To compute the derivative of U (we drop the index) w.r.t. M (and thus \mathcal{X}), one has to follow the chain rule:

$$\begin{aligned} \frac{\partial U}{\partial M_{kl}} &= \sum_{i,j} \frac{\partial U}{\partial (MM^T)_{ij}} \cdot \frac{\partial (MM^T)_{ij}}{\partial M_{kl}}, \\ \text{where } \frac{\partial u_{ij}}{\partial M^\#} &= u_{ij}(\lambda_{jj}\mathbb{I} - M^\#)^\dagger. \end{aligned} \quad (11)$$

Proposition 3. For SVD, we simply have to backpropagate through the chain rule:

$$\begin{aligned} \frac{\partial U \lambda U^T}{\partial X_{m'n'}} &= 2 \text{Sym} \left(\frac{\partial U}{\partial X_{m'n'}} \lambda U^T \right) + U \frac{\partial \lambda}{\partial X_{m'n'}} U^T, \\ \text{where } \text{Sym}(\mathbf{X}) &= \frac{1}{2}(\mathbf{X} + \mathbf{X}^T). \end{aligned} \quad (12)$$

Let $\mathbf{X} = U\lambda U^T$ be an SPD matrix with simple eigenvalues, i.e., $\lambda_{ii} \neq \lambda_{jj}, \forall i \neq j$, and U contain eigenvectors of matrix \mathbf{X} , then one can apply $\frac{\partial \lambda_{ii}}{\partial X} = \mathbf{u}_i \mathbf{u}_i^T$ and $\frac{\partial u_{ij}}{\partial X} = u_{ij}(\lambda_{jj}\mathbb{I} - \mathbf{X})^\dagger$.

Proof. The two rightmost steps $\frac{\partial \lambda_{ii}}{\partial X}$ and $\frac{\partial u_{ij}}{\partial X}$ are in [33]. \square

Proposition 4. For HOSVD, one has to follow the analogous chain rule as in Prop. 3, but expanded from Eq. (5). To obtain the der. of λ : a chain rule applies to Eq. (8).

4. Application to Action Recognition

Action Recognition pipelines. Powerful CNN architectures include the two-stream network [40], 3D spatio-temporal features [48, 50, 49, 42], spatio-temporal ResNet [13], GCN [37, 52, 53] and the I3D network pre-trained on Kinetics-400 [4]. However, these networks operate on the RGB and optical flow frames thus failing to capture some domain-specific information which sophisticated low-level representations capture by design. One prominent example are Improved Dense Trajectory (IDT) descriptors of [45] which are typically encoded with Bag-of-Words (BoW) of [41, 10] or Fisher Vectors (FV) of [34, 35] and fused with the majority of the modern CNN-based approaches of [16, 6, 7, 46, 8, 55, 51] at the classifier level for the best performance. Finally, attention in action recognition was also investigated in [18, 58, 54].

Improved Dense Trajectories. CNNs improve their performance if combined with IDT which involves several sophisticated steps: (i) camera motion estimation, (ii) modeling motion descriptors along motion trajectories captured with the optical flow, (iii) pruning inconsistent matches, (iv) removing focus from humans by the use of a human detector. IDT are usually combined with video descriptors such as Histogram of Oriented Gradients (HOG) [17, 21], Histogram of Optical Flow (HOF) [11] and Motion Boundary Histogram (MBH) [44] which are complementary to each other. Thus, we follow others and encode IDT descriptors by BoW/FV. Below we evaluate our tensor descriptors combined with EPN (and SigME which we call MaxExp in the reminder of the paper for simplicity as SigME is an extension of MaxExp to Krein spaces).

Our pipeline overview. Figure 3 introduces our action recognition pipeline. For each video sequence (an instance to classify), we first extract subsequences of lengths

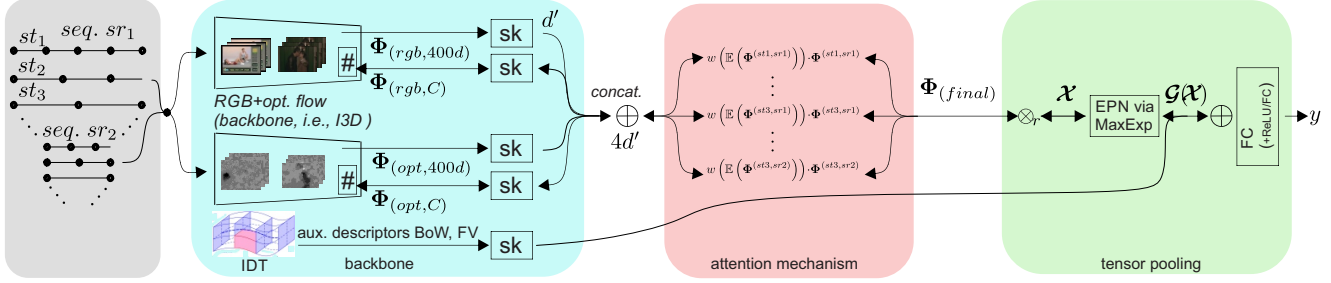


Figure 3: Our action recognition pipeline with the attention mechanism. See Section 4 for details.

st_1, \dots, st_3 with the stride equal half of the subsequence length. This allows our approach to attain an invariance to action localization. Moreover, we apply various sampling rates, *e.g.*, sr_1, sr_2 , which brings some invariance to the action speed. We pass each subsequence through two I3D networks [4] which were trained on the RGB and optical flow videos, respectively. For each network, we extract a 400 dimensional feature vector per subsequence whose coefficients coincide with the class labels of the Kinetics dataset (two-stream I3D CNN is pre-trained on Kinetics-400 off-the-shelf). Moreover, we use two more end-to-end trainable sub-streams of I3D denoted by (#) whose outputs are two C -dim. feature vectors per subsequence (*e.g.*, we backpropagate *w.r.t.* the last FC and the last inception block of I3D). Thus, we obtain intermediate matrices with feature vectors denoted as $\Phi(rgb, 400d)$, $\Phi(opt, 400d)$, $\Phi(rgb, C)$, and $\Phi(opt, C)$ which we pass through the count sketching mechanism from Appendix C, denoted (sk), to reduce the dimensionality to d' so that concatenating the corresponding feature vectors with (\oplus) results in the size of $4d' \approx 120$.

Attention mechanism. At this stage, we pass each group of feature vectors $\Phi^{(i,j)}$ by an attention mechanism, *i.e.*, $\Phi_w^{(i,j)} = w(\mathbb{E}(\Phi^{(i,j)})) \cdot \Phi^{(i,j)}$, where $i \in \{st_1, st_2, \dots\}$ and $j \in \{sr_1, sr_2, \dots\}$ are selectors of the step size and the sample rate, respectively. Moreover, an attention network $w: \mathbb{R}^{d'} \rightarrow \mathbb{R}$ takes a d' dim. expected value over a given group of feature vectors $\mathbb{E}(\Phi^{(i,j)})$ as input to produce an attention score within range $[0; 1]$. The attention network $w(\cdot)$ consists of an FC layer followed by a ReLU and another FC layer and a sigmoid function. The groups of feature vectors reweighted by such an attention mechanism form the final feature vector matrix $\Phi^{(final)} \in \mathbb{R}^{d \times N}$, where $d = 4d'$, which is then simply passed via Eq. (6). Finally, we obtain $\mathbf{X} \in \mathcal{S}_+^{d \times d}$ for $r=2$, or $\mathbf{X} \in \mathbb{R}^{d \times d \times d}$ for $r=3$, and we pass every \mathbf{X} via Eq. (3-5) to obtain $\mathcal{G}(\mathbf{X}) \in \mathbb{R}^{d \times d \times d}$, one per instance to classify. Finally, we combine our HoT descriptors with auxiliary descriptors (*e.g.*, IDT descriptors which are firstly count sketched (Appendix C) to reduce their dimensionality, and then concatenated with HoT), as our pipeline shows in Fig. 3.

| SO+ | $sp1$ | $sp2$ | $sp3$ | mean | TO+ | $sp1$ | $sp2$ | $sp3$ | mean |
|---------------------|-------|-------|-------|-------------|----------------------|-------|-------|-------|-------------|
| (no EPN) | 76.2 | 75.3 | 76.7 | 76.1 | (no EPN) | 75.4 | 74.0 | 75.0 | 74.8 |
| HDP | 81.4 | 78.8 | 80.1 | 80.1 | HDP | 81.8 | 79.6 | 81.3 | 80.9 |
| MaxExp | 81.7 | 79.1 | 80.1 | 80.3 | MaxExp | 82.3 | 79.9 | 81.2 | 81.1 |
| MaxExp+IDT | 86.1 | 85.2 | 85.8 | 85.7 | MaxExp+IDT | 87.4 | 86.7 | 87.5 | 87.2 |
| <hr/> | | | | | | | | | |
| ADL+ResNet+IDT [47] | 74.3 | | | | STM Network+IDT [14] | 72.2 | | | |
| | | | | | ADL+I3D [47] | 81.5 | | | |
| | | | | | Full-FT I3D [4] | | | | 81.3 |

Table 1: (*top*) Our model *vs.* (*bottom*) SOTA on HMDB-51.

| | <i>static</i> | <i>dynamic</i> | <i>mixed</i> | mean stat/dyn | mean all |
|---------------|---------------|----------------|--------------|------------------|-------------|
| SO+MaxExp | 92.52 | 82.03 | 89.44 | 87.3 | 88.0 |
| SO+MaxExp+IDT | 94.92 | 86.63 | 96.02 | 90.8 | 92.5 |
| TO+MaxExp+IDT | 95.36 | 86.90 | 97.04 | 91.1 | 93.1 |
| T-ResNet [15] | 92.41 | 81.50 | 89.00 | 87.0 | 87.6 |
| ADL I3D [47] | 95.10 | 88.30 | - | 91.7 | - |

Table 2: (*top*) Our pipeline *vs.* (*bottom*) SOTA on YUP++.

| | $sp1$ | $sp2$ | $sp3$ | $sp4$ | $sp5$ | $sp6$ | $sp7$ | mAP |
|----------------|-------|-------|-------|-------|-------|-------|-------|-------------|
| SO+MaxExp+IDT | 75.7 | 82.5 | 79.4 | 75.1 | 75.7 | 76.8 | 75.9 | 77.3 |
| TO+MaxExp+IDT | 78.6 | 83.4 | 81.5 | 78.8 | 81.7 | 79.2 | 79.6 | 80.4 |
| KRP-FS [7] | 70.0 | | | | | | | |
| KRP-FS+IDT [7] | 76.1 | | | | | | | |
| GRP [5] | 68.4 | | | | | | | |
| GRP+IDT [5] | 75.5 | | | | | | | |

Table 3: (*top*) Our pipeline *vs.* (*bottom*) SOTA on MPII.

5. Experiments

5.1. Datasets and Protocols

HMDB-51 [29] consists of 6766 internet videos over 51 classes; each video has ~ 20 –1000 frames. We report the mean accuracy (%) across three splits.

YUP++ [15] contains so-called video textures captured with the static or moving camera. It has 20 scene classes and 60 videos per class. We follow the standard splits (1/9 dataset for training) for the evaluation.

MPII Cooking Activities [39] has 64 activities in 3748 clips, *e.g.*, fine-grained actions *peel*, *slice*, *cut apart*. We use the mean Average Precision (mAP) over 7-fold crossvalidation. For human-centric protocol [7], we use Faster-RCNN [38] to crop video around humans.

Settings. For IDT, we applied PCA to trajectories (30 dim.), HOG (96 dim.), HOF (108 dim.), MBHx (96 dim.) and MBHy (96 dim.), and we obtained 213 dim. descriptors. We computed 1024 k-means and 256 dimensional GMM-based dictionaries, resp., and obtained 1024 and $\sim 110K$

final descriptors (FV was then count sketched to 4K). We used the Adam optimizer with $1e-4$ learning rate halved every 10 epochs. We ran our training for 50–200 epochs depending on the dataset. For second- and third-order descriptors, d (we say d but we mean $4d'$) was set within 200–1000 (400 for HMDB-51, 160 for YUP++, 520 for MPII) and $d \leq 150$ (80 for HMDB-51, 60 for YUP++, 60 for MPII), respectively. On HMDB-51/YUP++, we used two FC layers intertwined by a ReLU followed by a SoftMax classifier. On MPII, we used one FC (rightmost of Figure 3). Subsequence lengths were set to 48, 64, 80, 96, and sampling rates to 1, 2 (and 3 for HMDB-51/YUP++).

5.2. Evaluations

Firstly, we compare pipeline variants on HMDB-51. Table 1 shows that the second- and third-order pooling (SO) and (TO) without our eigenvalue/spectral MaxExp underperform, with (TO) being worse than (SO), as without MaxExp, third-order descriptors are poorly estimated. The accuracy between MaxExp and HDP differs by $\sim 0.25\%$ accuracy which validates our assumptions that EPN with MaxExp is in fact equivalent to the Heat Diffusion Process. Finally, third-order descriptors combined with MaxExp and IDT achieve 87.2% accuracy and outperform (SO) by 1.5%.

Table 2 shows that the accuracy on YUP++ obtained by third-order descriptors (TO) is $\sim 0.6\%$ higher than the accuracy of (SO). Results on YUP++ are close to saturation thus we do not expect big gains, yet we outperform other methods in the literature, e.g., T-ResNet of [15] by 5.6%.

Table 3 shows the results on MPII. For MPII, we have applied human-centric crops and used both IDT and I3D auxiliary features (I3D network was used with subsequences and global sequences subsampled to length 64). The third-order descriptor scored 80.4% mAP vs. 77.3% attained by second-order pooling. We note that with $d=520$ and $d=60$ (we say d but we mean $4d'$ here), second- and third-order descriptors contained 135K and 37820 unique coefficients, respectively. Decreasing d for second-order descriptors did not help improve results which shows the benefit of third-order descriptors. Our best score gains $\sim 4.9\%$ over the state-of-the-art GRP+IDT method.

6. Conclusion

We have established a connection between Eigenvalue Power Normalization via the MaxExp operator with the Heat Diffusion Process. We have shown that MaxExp approximates HDP but does not require the Laplacian matrix. We have applied MaxExp to higher-order tensor descriptors and obtained Tensor Power Normalization metric endowed with $\binom{d}{r}$ ‘detectors’ of the likelihood if at least one higher-order occurrence is ‘projected’ into one of $\binom{d}{r}$ subspaces of dimension r represented by the tensor. Our experiments on

action recognition show that third-order descriptors outperform second-order.

References

- [1] V. Arsigny, P. Fillard, X. Pennec, and N. Ayache. Log-euclidean metrics for fast and simple calculus on diffusion tensors. *Magnetic resonance in medicine*, 56(2):411–421, 2006. 2
- [2] Y. Boureau, J. Ponce, and Y. LeCun. A Theoretical Analysis of Feature Pooling in Vision Algorithms. *ICML*, 2010. 1
- [3] J. Carreira, R. Caseiro, J. Batista, and C. Sminchisescu. Semantic Segmentation with Second-Order Pooling. *ECCV*, 2012. 1
- [4] J. Carreira and A. Zisserman. Quo Vadis, Action Recognition? A New Model and the Kinetics Dataset. *CVPR*, pages 1–10, 2018. 5, 6
- [5] A. Cherian, B. Fernando, M. Harandi, and S. Gould. Generalized rank pooling for action recognition. In *CVPR*, 2017. 6
- [6] A. Cherian, P. Koniusz, and S. Gould. Higher-order pooling of cnn features via kernel linearization for action recognition. In *WACV*, 2017. 5
- [7] A. Cherian, S. Sra, S. Gould, and R. Hartley. Non-linear temporal subspace representations for activity recognition. In *CVPR*, pages 2197–2206, 2018. 5, 6
- [8] V. Choutas, P. Weinzaepfel, J. Revaud, and C. Schmid. Position: Pose motion representation for action recognition. In *CVPR*, pages 7024–7033, 2018. 5
- [9] G. Cormode and M. Hadjieleftheriou. Finding frequent items in data streams. *Proc. VLDB Endow.*, 1(2):1530–1541, Aug. 2008. 9
- [10] G. Csurka, C. R. Dance, L. Fan, J. Willamowski, and C. Bray. Visual categorization with bags of keypoints. *ECCV Workshop*, pages 1–22, 2004. 5
- [11] N. Dalal, B. Triggs, and C. Schmid. Human Detection Using Oriented Histogram of Flow and Appearance. *ECCV*, pages 428–441, 2006. 5
- [12] I. L. Dryden, A. Koloydenko, and D. Zhou. Non-euclidean statistics for covariance matrices, with applications to diffusion tensor imaging. *The Annals of Applied Statistics*, 3(3):1102–1123, 2009. 3
- [13] C. Feichtenhofer, A. Pinz, and R. P. Wildes. Spatiotemporal residual networks for video action recognition. In *NIPS*, pages 3468–3476, 2016. 5
- [14] C. Feichtenhofer, A. Pinz, and R. P. Wildes. Spatiotemporal multiplier networks for video action recognition. In *CVPR*, 2017. 6
- [15] C. Feichtenhofer, A. Pinz, and R. P. Wildes. Temporal residual networks for dynamic scene recognition. In *CVPR*, 2017. 6, 7
- [16] B. Fernando and S. Gould. Learning end-to-end video classification with rank-pooling. In *ICML*, volume 48, pages 1187–1196, 2016. 5
- [17] W. T. Freeman and M. Roth. Orientation histograms for hand gesture recognition. Technical Report TR94-03, MERL - Mitsubishi Electric Research Laboratories, Cambridge, MA 02139, Dec. 1994. 5

- [18] R. Girdhar and D. Ramanan. Attentional pooling for action recognition. In *NeurIPS*, 2017. 5
- [19] K. Guo, P. Ishwar, and J. Konrad. Action recognition from video using feature covariance matrices. *Trans. Img. Proc.*, 22(6):2479–2494, 2013. 1
- [20] M. Harandi, R. Hartley, C. Shen, B. Lovell, and C. Sander-son. Extrinsic methods for coding and dictionary learning on grassmann manifolds. *IJCV*, 2015. 2, 9
- [21] A. Klaser, M. Marszalek, and C. Schmid. A Spatio-Temporal Descriptor Based on 3D-Gradients. *BMCV*, pages 1–10, 2008. 5
- [22] T. G. Kolda and B. W. Bader. Tensor decompositions and applications. *SIAM Review*, 51(3):455–500, 2009. 2, 3
- [23] P. Koniusz and A. Cherian. Sparse coding for third-order super-symmetric tensor descriptors with application to texture recognition. In *CVPR*, 2016. 1, 2
- [24] P. Koniusz, Y. Tas, and F. Porikli. Domain adaptation by mixture of alignments of second- or higher-order scatter tensors. In *CVPR*, pages 7139–7148, 2017. 2
- [25] P. Koniusz, L. Wang, and A. Cherian. Tensor representations for action recognition. In *TPAMI*. IEEE, 2020. 1, 2
- [26] P. Koniusz, F. Yan, P. Gosselin, and K. Mikolajczyk. Higher-order occurrence pooling for bags-of-words: Visual concept detection. *PAMI*, 2016. 1, 2
- [27] P. Koniusz and H. Zhang. Power normalizations in fine-grained image, few-shot image and graph classification. In *TPAMI*. IEEE, 2020. 2, 3, 4
- [28] P. Koniusz, H. Zhang, and F. Porikli. A deeper look at power normalizations. In *CVPR*, pages 5774–5783, 2018. 2, 3
- [29] H. Kuehne, H. Jhuang, E. Garrote, T. Poggio, and T. Serre. Hmdb: a large video database for human motion recognition. In *ICCV*, pages 2556–2563. IEEE, 2011. 6
- [30] L. D. Lathauwer, B. D. Moor, and J. Vandewalle. A multilinear singular value decomposition. *SIAM J. Matrix Analysis and Applications*, 21:1253–1278, 2000. 2, 3
- [31] P. Li and Q. Wang. Local log-euclidean covariance matrix (l^2 ecm) for image representation and its applications. *ECCV*, 2012. 1
- [32] T.-Y. Lin and S. Maji. Improved Bilinear Pooling with CNNs. *BMVC*, 2017. 3
- [33] J. R. Magnus. On differentiating eigenvalues and eigenvectors. *Econometric Theory*, 1985. 5
- [34] F. Perronnin and C. Dance. Fisher kernels on visual vocabularies for image categorization. *CVPR*, 0:1–8, 2007. 5
- [35] F. Perronnin, J. Sánchez, and T. Mensink. Improving the Fisher Kernel for Large-Scale Image Classification. *ECCV*, pages 143–156, 2010. 5
- [36] F. Porikli and O. Tuzel. Covariance tracker. *CVPR*, 2006. 1
- [37] Z. Qin, Y. Liu, P. Ji, D. Kim, L. Wang, R. McKay, S. Anwar, and T. Gedeon. Fusing higher-order features in graph neural networks for skeleton-based action recognition. *IEEE Transactions on Neural Networks and Learning Systems*, 2022. 5
- [38] S. Ren, K. He, R. Girshick, and J. Sun. Faster r-cnn: Towards real-time object detection with region proposal networks. In *NIPS*, pages 91–99, 2015. 6
- [39] M. Rohrbach, S. Amin, M. Andriluka, and B. Schiele. A database for fine grained activity detection of cooking activities. In *CVPR*, 2012. 6
- [40] K. Simonyan and A. Zisserman. Two-stream convolutional networks for action recognition in videos. In *NIPS*, pages 568–576, 2014. 5
- [41] J. Sivic and A. Zisserman. Video Google: A text retrieval approach to object matching in videos. *ICCV*, 2:1470–1477, 2003. 5
- [42] D. Tran, L. Bourdev, R. Fergus, L. Torresani, and M. Paluri. Learning Spatiotemporal Features with 3D Convolutional Networks. *ICCV*, pages 4489–4497, 2015. 5
- [43] O. Tuzel, F. Porikli, and P. Meer. Region covariance: A fast descriptor for detection and classification. *ECCV*, 2006. 1
- [44] H. Wang, A. Klaser, C. Schmid, and C.-L. Liu. Dense Trajectories and Motion Boundary Descriptors for Action Recognition. *IJCV*, 2013. 5
- [45] H. Wang and C. Schmid. Action Recognition with Improved Trajectories. *ICCV*, pages 3551–3558, 2013. 5
- [46] J. Wang and A. Cherian. Learning discriminative video representations using adversarial perturbations. In *ECCV*, pages 716–733, 2018. 5
- [47] J. Wang and A. Cherian. Learning discriminative video representations using adversarial perturbations. In *ECCV*, 2018. 6
- [48] L. Wang. Analysis and evaluation of Kinect-based action recognition algorithms. Master’s thesis, School of the Computer Science and Software Engineering, The University of Western Australia, Nov 2017. 5
- [49] L. Wang, D. Q. Huynh, and P. Koniusz. A comparative review of recent kinect-based action recognition algorithms. *TIP*, 2019. 5
- [50] L. Wang, D. Q. Huynh, and M. R. Mansour. Loss switching fusion with similarity search for video classification. *ICIP*, 2019. 5
- [51] L. Wang and P. Koniusz. Self-supervising action recognition by statistical moment and subspace descriptors. In *ACM-MM*, pages 4324–4333, 2021. 5
- [52] L. Wang and P. Koniusz. Temporal-viewpoint transportation plan for skeletal few-shot action recognition. In *ACCV*, pages 4176–4193, 2022. 5
- [53] L. Wang and P. Koniusz. Uncertainty-dtw for time series and sequences. In *ECCV*, pages 176–195. Springer, 2022. 5
- [54] L. Wang and P. Koniusz. 3mformer: Multi-order multi-mode transformer for skeletal action recognition. In *CVPR*, pages 5620–5631, 2023. 5
- [55] L. Wang, P. Koniusz, and D. Huynh. Hallucinating idt descriptors and i3d optical flow features for action recognition with cnns. In *ICCV*, pages 8697–8707, 2019. 5
- [56] Q. Wang, F. Chen, and W. Xu. Tracking by third-order tensor representation. *Systems, Man, and Cybernetics, Part B: Cybernetics, IEEE Transactions on*, 41(2):385–396, 2011. 1
- [57] K. Weinberger, A. Dasgupta, J. Langford, A. Smola, and J. Attenberg. Feature hashing for large scale multitask learning. In *ICML*, pages 1113–1120, 2009. 9
- [58] Y. Zhang, S. Tang, K. Muandet, C. Jarvers, and H. Neumann. Local temporal bilinear pooling for fine-grained action parsing. In *CVPR*, pages 12005–12015, 2019. 5

High-order Tensor Pooling with Attention for Action Recognition (Supplementary Material)

Piotr Koniusz^{§,†} Lei Wang^{†,§} Ke Sun^{§,†}
[†]Australian National University, [§]Data61/CSIRO
[§]firstname.lastname@data61.csiro.au

A. Proof of Remark 1

Proof. It trivially follows that $\mathcal{G}(\mathbf{X}) = \mathbf{U} \text{diag}(g(\boldsymbol{\lambda})) \mathbf{U}^T = \mathbf{U}_{:,1:q} \mathbf{U}_{:,1:q}^T$ from the definition of g which acts as a selector of eigenvectors corresp. to q largest eigenvalues. This results coincides with the feature map of the Grassmann distance, *e.g.*, see [20]. \square

B. Proof of Theorem 1

Proof. The proof follows the fair coin toss syllabus. The probability of all N outcomes to be $\{(\psi_1 = 0), \dots, (\psi_N = 0)\}$ amounts to $(1-p)^N$. The probability of at least one positive outcome $(\psi_n = 1)$ amounts to applying the logical ‘or’ $\{(\psi_1 = 1) \mid \dots \mid (\psi_N = 1)\}$ which yields $1 - (1-p)^N = \sum_{n=1}^N \binom{N}{n} p^n (1-p)^{N-n}$. \square

C. Count Sketches

Sketching feature vectors by the count sketch of [9, 57] is used for their dimensionality reduction in this paper.

Proposition 5. *Let d and d' denote the input and output dimensionality of the input and sketched output vectors, respectively. Let vector $\mathbf{h} \in \mathcal{I}_{d'}^d$ contain d uniformly drawn integer numbers from $\{1, \dots, d'\}$ and vector $\mathbf{s} \in \{-1, 1\}^d$ contain d uniformly drawn values from $\{-1, 1\}$. Then, the sketch proj. matrix $\mathbf{P} \in \{-1, 0, 1\}^{d' \times d}$ becomes $P_{ij} = s_i$ if $h_i = j$, 0 otherwise, and the sketch proj. $sk : \mathbb{R}^d \rightarrow \mathbb{R}^{d'}$ is a linear operation given as $sk(\phi) = \mathbf{P}\phi$.*

Proof. Follows directly from the Definition 1 in the paper of [57]. \square